Advanced Coherent X-Ray Diffraction and Electron Microscopy of Individual InP Nanocrystals on Si Nanotips for III-V-on-Si Electronics and Optoelectronics

Gang Niu,[1,*] Steven John Leake,[2,†] Oliver Skibitzki,[3] Tore Niermann,[4] Jerome Carnis,[2,5] Felix Kießling,[4] Fariba Hatami,[6] Emad Hameed Hussein,[6] Markus Andreas Schubert,[3] Peter Zaumseil,[3] Giovanni Capellini,[3,7] William Ted Masselink,[6] Wei Ren,[1] Zuo-Guang Ye,[1,8] Michael Lehmann,[4] Tobias Schülli,[2] Thomas Schroeder,[4,9,‡] and Marie-Ingrid Richard[2,5,§]

[1] *Electronic Materials Research Laboratory, Key Laboratory of the Ministry of Education & International Center for Dielectric Research, School of Electronic Science and Engineering, Xi'an Jiaotong University, Xi'an 710049, China*

[2] *ESRF – The European Synchrotron, 71 Avenue des Martyrs, 38000 Grenoble, France*

[3] *IHP-Leibniz-Institut für innovative Mikroelektronik, Im Technologiepark 25, 15236 Frankfurt (Oder), Germany*

[4] *Technische Universität Berlin, Institut für Optik und Atomare Physik, Straße des 17. Juni 135, 10623 Berlin, Germany*

[5] *IM2NP UMR 7334, Aix Marseille Université, CNRS, Université de Toulon, F-13397 Marseille, France*

[6] *Institut für Physik, Mathematisch-Naturwissenschaftliche Fakultät, Humboldt Universtät zu Berlin, Newtonstrasse 15, 12489 Berlin, Germany*

[7] *Dipartimento di Scienze, Università Roma Tre, Viale Marconi 446, 00146 Rome, Italy*

[8] *Department of Chemistry and 4D LABS, Simon Fraser University, Burnaby, British Columbia V5A 1S6, Canada*

[9] *Brandenburgische Technische Universität, Konrad-Zuse-Strasse 1, 03046 Cottbus, Germany*

(Received 8 March 2019; revised manuscript received 17 April 2019; published 19 June 2019; corrected 2 August 2019)

The nondestructive detection and evaluation of crystallographic properties of nanocrystals is of great significance for both fundamental physics research and further development of high-performance functional devices employing nanostructured materials. Synchrotron radiation-based CXD using a nanoscale x-ray beam is shown to be a powerful tool to explore the crystallographic properties of InP nanocrystals (NCs) selectively grown on Si nanotip wafers. CXD characterization clearly clarifies, with atomic sensitivity and without complex sample preparation, the crystallographic properties of the selected InP NC such as the structure of the facets, the strain, the existence of defects (stacking faults and microtwins), and the size of the defected crystallites. Several selected InP NCs explored by CXD reveal homogeneous structures. The CXD results are in good agreement with electron microscopy. These results not only confirm that nanoheteroepitaxy is a promising approach to monolithically integrate high-quality III-V compounds on silicon wafers, but also opens a pathway to nondestructively explore the crystallinity of materials on the nanometer scale, particularly in nano-electronic and nano-optoelectronic devices.

DOI: 10.1103/PhysRevApplied.11.064046

I. INTRODUCTION

In crystals, defects and strain play an important role in the definition of a material's properties and thus its performance when integrated into functional devices [1–5]. Nanostructured crystals by definition are complex. And despite recent developments of both electron and x-ray techniques, the challenge remains to investigate the crystallinity of nanocrystals (NCs) in three dimensions with high resolution and *operando*. III-V compounds on Si represent typical industrially relevant heterogeneous epitaxial systems, III-V compounds are exploited in high-mobility channels in higher speed and lower power complementary-metal-oxide-semiconductor (CMOS) devices, and are used as light sources for on-chip and interchip optical interconnects [6–8]. The III-V/Si systems typically exhibit defects including dislocations, stacking faults (SFs), and antiphase domains (APDs).

InP is one of the most common III-V compounds and has been widely studied for various applications [9,10], such as heterojunction bipolar transistors (HBTs), solar cells, photodetectors, lasers, optical generators, switching and detection components, and so on. Among the strategies attempting to improve the crystalline quality of III-V-on-Si substrates [7,11–15], the nanoheteroepitaxy

*gangniu@xjtu.edu.cn
†steven.leake@esrf.fr
‡thomas.schroeder@ikz-berlin.de
§mrichard@esrf.fr

 © 2019 American Physical Society

of III-V compounds on patterned Si wafers has recently been demonstrated as a promising approach to realize high-quality III-V NCs with low-density defects [16–20]. In particular, one of our prior studies [17] showed that InP NCs selectively grown on a Si nanotip wafer possess a similar optoelectronic property as the InP bulk reference sample. However, InP NCs at nanometric dimensions and the ease with which InP NCs grown on Si tips detach make the commonly used characterization by laboratory-based XRD and TEM even more difficult and challenging.

Coherent diffraction imaging (CDI) is a lens-less far-field imaging technique, allowing the reconstruction of an object in direct space using phase retrieval methods on the Fraunhofer diffraction pattern recorded in the vicinity of a Bragg reflection [21–24]. The resulting complex object has both an amplitude, the electron density scattering to the specific Bragg peak, and a phase, which describes the displacement field of the lattice relative to a perfect lattice with sub-angstrom sensitivity. In particular, when used with an x-ray beam rather than electrons, CDI can look inside crystals in three dimensions without changing the native state of the sample. Therefore, since its first experimental demonstration in 1999 by Miao *et al.* [25], CDI has been widely and successfully employed for the exploration of perfect NCs with very small strain [26–29]. More recently, the capability of CDI to evaluate the strain state and defects in nanostructures has also been demonstrated [21,23,24,30–35].

In this work, we employ CXD to reveal the structure of InP nanocrystals by exploiting the coherent properties of the x-rays. Single crystalline InP NCs are selectively grown on patterned Si nanotips wafers via MBE. CXD is performed on different single InP NCs. First, we demonstrate that the CXD result on a selected InP NC is well explained by combining the SEM images on the same nanocrystal. Synchrotron-based grazing incidence XRD (GIXRD) and TEM analysis are also carried out and the results agree well with the CXD insights. It is revealed that the InP NC with a diameter of approximately 350 nm is monocrystalline with defects such as SFs and nanotwins, and it is entirely relaxed on the Si nanotip. The details of SFs and nanotwins are also revealed by CXD. A second selected InP NC particle is characterized by CXD. This particle is slightly compressed (−0.5%) with respect to bulk InP. We succeed in applying phase retrieval and thus get an image (CDI) of the particle in direct space. A twinned crystal is retrieved in agreement with TEM. The CXD and CDI results confirm that nanoheteroepitaxy (NHE) is a highly promising approach to grow high quality III-V materials on silicon substrates, which is of great significance for the monolithic integration of III-V compounds on a Si-CMOS platform. CXD as well as CDI turn out to be powerful tools to nondestructively characterize crystal size, facet shape, strain, and defects in InP nanocrystals, which thus opens a pathway for the advanced characterization of crystallographic properties of nanostructured materials even in fully processed devices in the future.

II. EXPERIMENT

A Riber 32P gas-source molecular beam epitaxy system is employed to heteroepitaxially grow InP NCs on patterned Si nanotip wafers, which are fabricated in a standard 0.25-μm CMOS process line. The Si nanotip substrate contains a square matrix of crystalline "Si seeds" emerging in an amorphous SiO_2 layer. The diameter of crystalline Si seeds is controlled by a chemical mechanical polishing (CMP) process and is approximately 60 nm in this study. More details of the fabrication of Si nanotips can be found in Refs. [36] and [37]. In order to remove the native SiO_2 on Si seeds, the Si nanotips substrate is prebaked at 800°C for 5 min in ultrahigh vacuum (UHV) of the MBE chamber prior to the InP growth. The InP is grown by cosupplying evaporated solid In and thermally cracked phosphine gas (PH_3). To achieve the selective growth of InP on Si nanotips without nucleating on the SiO_2 surface, low-growth rates of 0.3–1.6 Å/s combined with a high-growth temperature of approximately 500°C and high P/In ratios are used. A Zeiss Nvision SEM is used to examine the surface morphology and facets of InP NCs. In order to prevent the charging effect induced by the insulating SiO_2 layer, a low electron beam energy of 1.5 keV is used. The sample crystallinity and the epitaxy of InP are confirmed by a laboratory-based Rigaku Smartlab diffractometer with a 9-kW rotating anode (Cu $K\alpha 1$, $\lambda = 1.5406$ Å). Synchrotron radiation-based grazing incidence x-ray diffraction (SR GIXRD) is performed at bending magnet 32, interface (BM32) beamline at European Synchrotron Radiation Facility (ESRF) with an x-ray wavelength of 1.127 Å. In order to detect the crystallinity of an individual InP NC, TEM measurements are carried out by the FEI TITAN 80-300 Berlin Holography special microscope operated at 300 kV and the lamellas are prepared with a focused ion beam after covering the InP NCs with a carbon layer to avoid possible deformation of InP NCs and Si nanotips (Supplemental Material) [58]. CXD measurements are performed at the insertion device 01, microdiffraction imaging (ID01) beamline at ESRF. A coherent portion [60 μm (Horizontal, H) × 200 μm (Vertical, V)] of the monochromatic (8.0 keV) beam is selected by using high precision slits. The coherent x-ray beam is then focused to 100 nm (V) × 300 nm (H) by a Fresnel Zone Plate (FZP) with a diameter of 300 μm. The diffraction patterns are collected by a two-dimensional (2D) Maxipix detector with a 516 × 516 array of 55 × 55 micrometer sized pixels. Initially, a K map scan is performed at the Bragg conditions of InP (002) (Bragg angle of 15.2°) to locate InP NCs [38]. Then a specific target InP NC is chosen and a coherent nano x-ray beam,

with dimensions similar to the crystals, is used to record three-dimensional (3D) reciprocal space maps by rotating the sample in a range of 2° with a step size of 0.0077°, detailing the intensity distribution local to the Bragg peak. A scan for one single InP NC takes approximately 10 min.

III. RESULTS AND DISCUSSION

The global morphology and crystalline structure of the InP NCs are characterized. The morphology of the InP NCs grown on Si nanotip wafers is examined by SEM and the results are shown in Fig. 1. Figure 1(a) is a side-view (60° tilt) SEM image showing the InP NCs array and a cross-section view of the Si nanotip wafer at the bottom part. The cross section is along the Si [110] direction. The crystalline Si seeds, which emerge in the amorphous SiO_2 layer, possess a circular shape with a diameter of approximately 60 nm. The tip array square edge is along the Si [100] direction and the tip-tip distance is 1.41 μm (more details on Si nanotip wafers can be found in the Supplemental Material) [58]. It can be seen in Fig. 1(a) that InP NCs are entirely selectively grown on Si nanotips without the observation of droplets on the SiO_2 region thanks to the optimized growth conditions described previously. The InP NCs are nominally 350 nm in diameter, which is consistent with the targeted thickness, and confirms these particular growth conditions lie in the so-called diffusion-limited region [39]. Here, the In atoms, which arrive directly on the crystalline Si seeds, contribute to the growth of InP NCs while the In adatoms, which fall onto the SiO_2 layer (with a short diffusion length) are reevaporated [40,41] (Supplemental Material) [58]. Figure 1(b) shows an enlarged SEM image (80° tilted) of 18 InP NCs, which exhibit distinct facets. Our InP NCs mainly show {001}, {110}, and {111} facets. However, this behavior is different from the equilibrium crystalline shape (ECS) of coherently strained InP crystals showing well-ordered {110}, {111} facets and a (001) top surface [42]. This can be understood by the fact that the MBE growth is far from equilibrium and our InP NCs are probably relaxed because of the 3D strain relief in NHE via the island edges [16].

Due to the nanometer size and the small amount of the InP NC material, the laboratory-based XRD measurements suggest that the InP is (001)-oriented single crystalline; however, the intensity of InP Bragg peaks is very low, making the analysis of crystallinity rather challenging (Fig. S1 within the Supplemental Material) [58]. In order to clarify the crystallinity of the InP NCs, SR-GIXRD is, therefore, carried out at the BM32 beamline of ESRF and the results are shown in Figs. 1(c) and 1(d). In GIXRD, during a θ–2θ scan, both the sample and detector are moved. This allows to probe the strain inside a sample. During an ω scan, the sample is rotated at a fixed detector position. The measurement is performed at a fixed strain position. Figure 1(c) shows the θ–2θ measurement in the

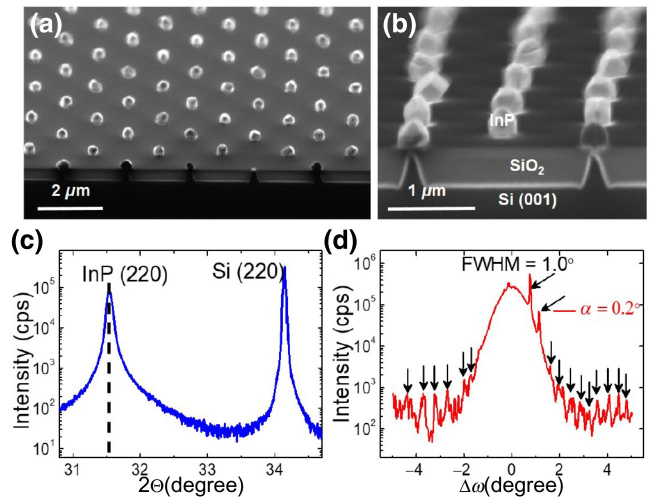

FIG. 1. Global properties of InP NCs on the Si nanotips wafer. (a) A side-view SEM image (60° tilt from top view), which shows a cross section along the Si [110] direction of the heterostructure as well. The darkest regions are Si and the filling material between Si nanotips is SiO_2. The tip array square edge is along the Si [100] direction and the tip-tip distance is 1.41 μm. (b) An enlarged SEM image in side-view (80° tilt from top view) of the sample in (a), showing eighteen InP NCs. SR-GIXRD patterns of InP NCs detected at BM32 beamline of ESRF ($\lambda = 1.127$ Å). (c) θ–2θ scan around the Si (220) Bragg diffraction in-plane condition; the black dotted lines mark the (220) peak position of bulk InP. (d) ω scan of InP (220) diffraction peak with the x-ray incident angle α of 0.2°, showing a FWHM of 1.0°. The black arrows mark diffraction peaks related to InP NCs relatively strongly twisted to the substrate.

vicinity of the Si (220) Bragg diffraction condition. Along with the Si (220) Bragg peak at $2\theta = 34.14°$, a strong peak appears at $2\theta = 31.53°$, corresponding to the cubic InP (220) reflection. The InP (220) reflection indicates a sharp single-peak feature and locates exactly on the peak position of bulk InP with a zincblende structure (marked by the black dashed line). This result suggests that the InP NCs are completely strain relaxed. It is well-known that the strain in lattice-mismatched heterosystems can be released by forming defects such as dislocations and SFs. On the other hand, NHE allows elastic strain relaxation via the strain release at the edge of NCs in a 3D manner and possible strain partitioning between the InP NC and the Si nanotip [16,37,43]. Therefore, the angular or ω scan of the InP (220) Bragg diffraction peak measured at an incident angle α of 0.2° is carried out to further explore the crystallinity of the InP NCs, as shown in Fig. 1(d). The FWHM of the InP (220) peak is approximately 1.0°, which is significantly larger than that (approximately 0.02°) of the perfect InP crystals with a size of approximately 350 nm. Therefore, the InP NCs on Si nanotips demonstrate mosaicities, that is, lattice tilt and twist, possibly induced by defects like microtwins (μTWs), SFs, and dislocations. It is worth

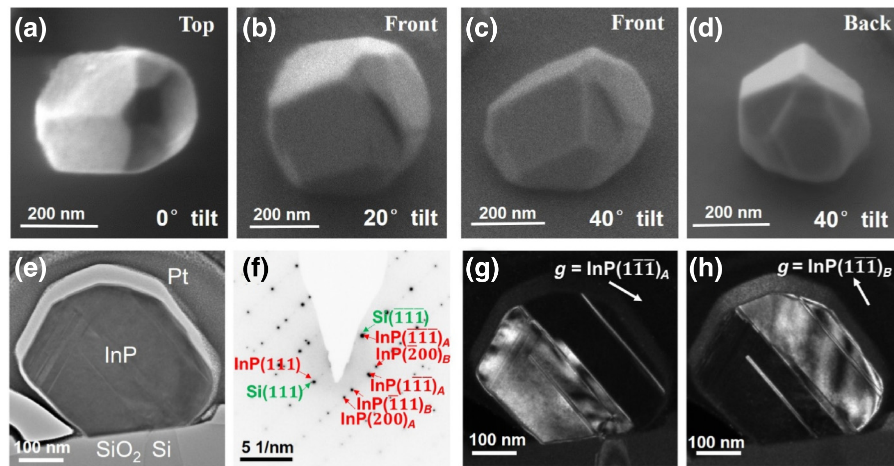

FIG. 2. SEM and TEM images of a single InP NC heterogeneously epitaxially grown on a Si nanotip. SEM images of one selected InP NC showing its detailed surface morphology: (a) top view; (b) 20° tilt from top view of the same InP NC, named "Front"; (c) 40° tilt from top view of the same InP NC, still at "Front"; (d) 40° tilt from top view of the same InP NC with the InP NC rotated nearly 180° in the plane, named "Back". TEM images of another InP NC: (e) a HRTEM cross-section image showing the crystalline feature of InP with μTWs. The top Pt layer is deposited before the FIB process to protect the InP NC from detaching from the Si nanotip. (f) A selected area electron diffraction pattern of the InP/Si system. The InP reflections indexed by *A* and *B* belong to different twin variants, the [111] direction is common. DF TEM images from reflections exclusive to the individual variants are shown in (g) and (h).

pointing out that the broadening of the InP (220) peak is more probably caused by the slightly different orientation of different NCs. In Fig. 1(d), sharp small peaks (marked by black arrows) also appear, which are expected to be the diffraction of individual InP NCs with relatively strong misorientation to the substrate**.**

The morphology of a single InP NC is further studied by both SEM and CXD to explore in detail the typical faceted structure of InP NCs. Figure 2(a) shows a top-view SEM image of a selected InP NC, which has {110} and {111} facets possessing lowest surface energies. Figure 2(b) displays a 20° tilted SEM image with the "Front" side. Figures 2(c) and 2(d) show 40° tilted SEM images showing the "Front" and "Back" sides, respectively, of the very same InP NC shown in (a) and (b). The InP NC does not show the equilibrium crystal shape (ECS) anticipated for a coherently strained NC, which minimizes the surface energy through a Wulff construction [44], probably due to the strain relaxation via the NHE method and/or the formation of defects such as SFs and μTWs. More SEM images for other selected InP NCs can be found in Fig. S5 within the Supplemental Material [58].

To identify the defects present in InP NCs, TEM measurements are carried out. The results are presented in Fig. 2. It should be noted here that due to the destructive nature of the TEM lamella preparation, the preparation methods including ion milling and focused ion beam (FIB) are not completely suitable for such III-V/Si heterostructures (Supplemental Material) [58]. The InP NCs tend to detach from the Si nanotips while the top of the Si nanotip tends to be bent during the lamella preparation. The TEM lamellas are, therefore, prepared by initially depositing a protective platinum layer within the FIB to **"**fix" the InP NCs, followed by the conventional FIB lamella preparation. Figure 2(e) displays a cross-section TEM image of the InP/Si nanotip heterostructure and indicates that a crystalline InP NC is grown on a Si nanotip with a diameter of approximately 60 nm. Such a small lateral size of Si crystalline seed would increase the critical thickness of epitaxial films in a heterogeneous system [16]. No threading dislocations can be found in InP NC; however, twin boundaries are visible. In the InP NC shown in Fig. 2(e), two large area twins dominate the volume, while on the top left, some smaller twinned regions and SFs can be seen. Figure 2(f) shows a selective area electron diffraction (SAED) pattern of the studied InP/Si nanotip system. It confirms that the residual strain of the InP NC is less than 1%. As indicated by indices A and B, InP diffraction dots belonging to two twin variants are observable, while the InP (111) reflections (and multiples) are common to both variants. The twin variants are visualized by dark field (DF) TEM images in Figs. 2(g) and 2(h) using reflections, which are exclusive to the variants. Furthermore, it can be observed that the two main SFs stem from the edges of the Si tip contacting SiO_2, where strain and composition fluctuations might exist [45]. For the InP material, the formation energy of μTWs compared with that for dislocations is known to be very low [46]. Thus μTWs mainly form at the edges of the Si tip and partly facilitate the release of lattice mismatch strain [47]. Due to the abrasive preparation method, we assume the internal defect structure remains the same, but we cannot infer much at the surfaces as modification

from its initial state cannot be ruled out. It is valuable to point out here that a detailed TEM study on strain relaxation as well as the defects in another III-V compound, that is, GaAs NCs grown on Si nanotips, has been reported by Kozak *et al.* [48]. Both InP/Si tips and GaAs/Si tips systems show rather similar behaviors.

In order to observe the structure of a single InP NC in a nondestructive manner in three dimensions, CXD measurements are carried out at the ID01 beamline at the ESRF. We first perform a scan of the beam across the sample and use diffraction contrast of the InP (002) reflection, the so called "*K* map" scan ($30 \times 30\ \mu m^2$), to locate InP NCs on the sample (Supplemental Material) [58]. These are correlated with optical microscope (OM) and SEM in order to compare the morphology (the faceted structure) revealed by SEM with the diffraction pattern measured with CXD. Figure 3(a) inset shows the SEM image of the selected InP NC, more details of which are shown in Figs. 2(a)–2(d). Figure 3(b) displays the (002) Bragg reflection of the corresponding selected InP NC as a function of the reciprocal space coordinates (Q_x, Q_y, and Q_z). The center of mass of the 3D diffraction pattern is located at $Q \approx 2.142$ Å^{-1}, leading to an out-of-plane lattice parameter of $c \approx 5.866$ Å, very close to the theoretical lattice parameter of InP ($a = 5.8687$ Å). This implies that the InP nanoparticle (NC1) on average is fully relaxed. Three well-defined streaks are observed. Two of them are along the $\langle 111 \rangle$ directions. Along these two streaks, fringes can be clearly observed [marked by the arrows in Figs. 3(b) and 3(c)]. NC1 is typical and representative in InP NCs. We examine more than 5 NCs and they show quite similar features. The 3D diffraction pattern of the second InP nanoparticle (NC2) is shown in Fig. 3(d). Its center of mass is located at $Q \approx 2.151$ Å^{-1}, leading to an out-of-plane lattice parameter of $c \approx 5.8388$ Å. In contrast to the NC1, which is fully relaxed, the NC2 on average is slightly compressed (−0.5%). The strain status of NC2 is slightly different from NC1 and from the result obtained by GIXRD globally detecting all NCs, which demonstrates the advantage of CXD for the detailed examination of individual InP NCs. Defined streaks are also observed. Two are along the $\langle 111 \rangle$ directions. It is known that a 3D CDI pattern can be theoretically calculated by summing the amplitudes scattered by each atom with its phase factor, using the following kinematic approximation:

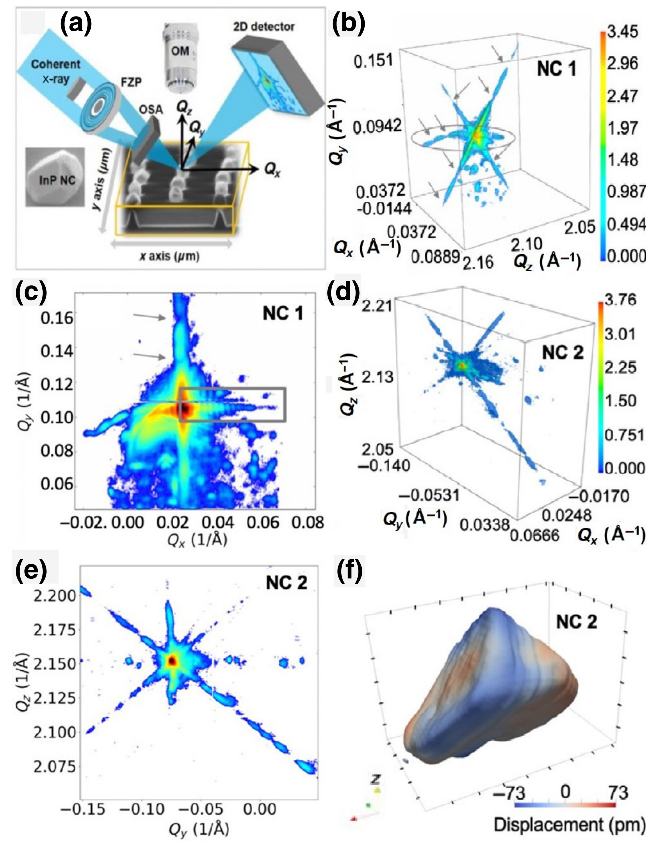

FIG. 3. (a) A schematic image of the CXD measurements configuration, in which FZP represents the Fresnel zone plate and OSA is the order sorting aperture. Left panel shows the SEM image of a selected InP NC. (b) 3D diffraction pattern of the selected InP NC shown in Fig. 2(a). The pattern displayed as a function of the reciprocal space coordinates (Q_x, Q_y and Q_z) in Angstroms and measured at the InP (002) Bragg reflection. The arrows mark the fringes with a large period and the oval circles the bent streak. (c) Summed diffraction pattern displayed in the (Q_x,Q_y) plane. (d) 3D diffraction pattern of NC 2 measured at the InP (002) Bragg reflection. (e) Summed diffraction pattern displayed in the (Q_y,Q_z) plane. (f) Isosurface of the out-of-plane displacement of the InP particle (NC 2). Here, a twin domain of the particle has been reconstructed. The distance between two ticks corresponds to 50 nm.

$$\mathbf{I}(\mathbf{q}) = \left| \sum\nolimits_j \mathbf{f}_j \exp\left(2i\pi \mathbf{q} \times \mathbf{r}_j\right) \right|^2, \qquad (1)$$

where $\mathbf{q}$ is the scattering vector, $\mathbf{f}_j$ is the atomic scattering factor, and $\mathbf{r}_j$ is the position of atom j. Here, we assume a plane wave illumination and fully coherent scattering whereas the atomic scattering factor, absorption, and refraction effects are not considered. According to Eq. (1), it can be seen that CDI is sensitive to the displacement even in the absence of strain. Therefore, CDI studies have been used to study numerous systems with multiple defects, such as InSb pillars with SFs [34], GaAs/GaP nanowires [30], and so on. Defects like dislocations, SFs, and μTWs all induce a global shift of one part of the nanocrystal from another, and thus phase changes in diffraction occur. For the InP NCs grown on Si nanotips using NHE, due to the small energy for the formation of SFs in InP [46], the strain induced by the lattice mismatch is mainly released by the formation of SFs or μTWs. Therefore, the principal defects in our InP NCs are SFs and μTWs. SFs (and μTWs' boundaries) are quite common in fcc crystals and usually occur

in the {111} planes [5]. The phase jump $\Delta\varphi$ across a SF (or a μTW boundary) is dominated by

$$\Delta\boldsymbol{\varphi} = \frac{2\pi}{3}\mathbf{n}_{111}(\mathbf{h}+\mathbf{k}+\mathbf{l}), \tag{2}$$

where $\mathbf{n}_{111}$ is the number of faulted planes. When $\mathbf{h}+\mathbf{k}+\mathbf{l}=3\mathbf{n}$ (e.g., for the {111} reflection), the phase jump is a multiple of 2π and the SF would be invisible, whereas when $\mathbf{h}+\mathbf{k}+\mathbf{l}\neq 3\mathbf{n}$ (e.g., in $\{11\bar{1}\}$ or {002} reflection), a SF (or a μTW boundary) causes a phase shift of $\pm 2\pi/3$ between the two sides of the SF, thus resulting in a strong signature in the diffraction pattern. The most significant signature of SFs is the reinforcement of the intensity on the streak along ⟨111⟩ with a modification of its fringes. A SF (or a μTW boundary) located in the middle of the studied crystal volume induces maximal destructive interference and a doubled period of the fringes. Therefore, by analyzing the distance of the fringes modified by the SF (or the μTW boundary), one can estimate the size of the crystallites separated by the μTWs [30,49].

Figures 3(b) and 3(c) display the diffraction patterns of NC1 as a function of Q_x, Q_y, and Q_z reciprocal space coordinates. The diffraction patterns show ⟨111⟩ streaks, which come either from {111} facets or {111}-type defects [like {111} SFs or twins, which are common in zincblende semiconductors]. In particular, in Fig. 3(c), along the Q_x axis, fringes with a short period (marked by a square) appear, which correspond to a distance of approximately 280 nm, the size of the InP NC. This is consistent with the SEM and TEM observations. Meanwhile, the fringes along the Q_y axis [marked by the arrows, similar to that shown in Fig. 3(b)] possess a larger period. These fringes correspond to 30 nm in direct space, which is much smaller than the size of the particle and correspond to the μTWs observed by TEM in Fig. 2. Interestingly, the third streak (marked by the orange oval) is an asymmetrical bent streak. This asymmetry is also a clear sign of a strong phase structure (hence, defect structure) of the SFs located at different positions in the crystal volume.

The diffraction pattern of NC2 is displayed in Figs. 3(d) and 3(e). ⟨111⟩ streaks are also observed. We succeed in performing CDI and retrieve the shape, displacement, and strain field of the measured crystal (more details in Supplemental Material) [50–56,58]. Figure 3(f) shows the reconstructed isosurface of the Bragg density colored by the out-of-plane atomic displacement from NC2 from the diffraction patterns displayed in Figs. 3(d) and 3(e). Interestingly, only one component of the crystal is reconstructed, demonstrating the presence of several crystal domains distinguished by orientation. The overall local out-of-plane displacement field and strain span over ±73 pm and 1%, respectively (see Supplemental Material) [58]. The imaged component of crystal has an average lateral size of approximately 250 nm and a height of approximately 325 nm and is consistent with the SEM and TEM observations.

In order to directly compare the faceting observed in SEM, we extract pole figures from the diffraction patterns, see Fig. 4 [57]. The NC1 and NC2 are shown in Figs. 4(a) and 4(b), respectively. The pole figures are centered on the position of the (001) pole as the (002) reflection has been measured. In the figure, poles of the {111} type (found at 54.74° along the polar direction and highlighted by black circles) and {100} type (highlighted by green circles) are observed. The poles correspond either to the intersection of ⟨111⟩ or ⟨100⟩ streaks with the sphere used for the stereographic projection. The streaks come from {111} or {100} facets of the NC. This confirms the facets observed in SEM in Fig. 2 and the fact that some of the fringes are bent gives rise to the nonuniform distribution of the {111} facets. Note that SFs and twins

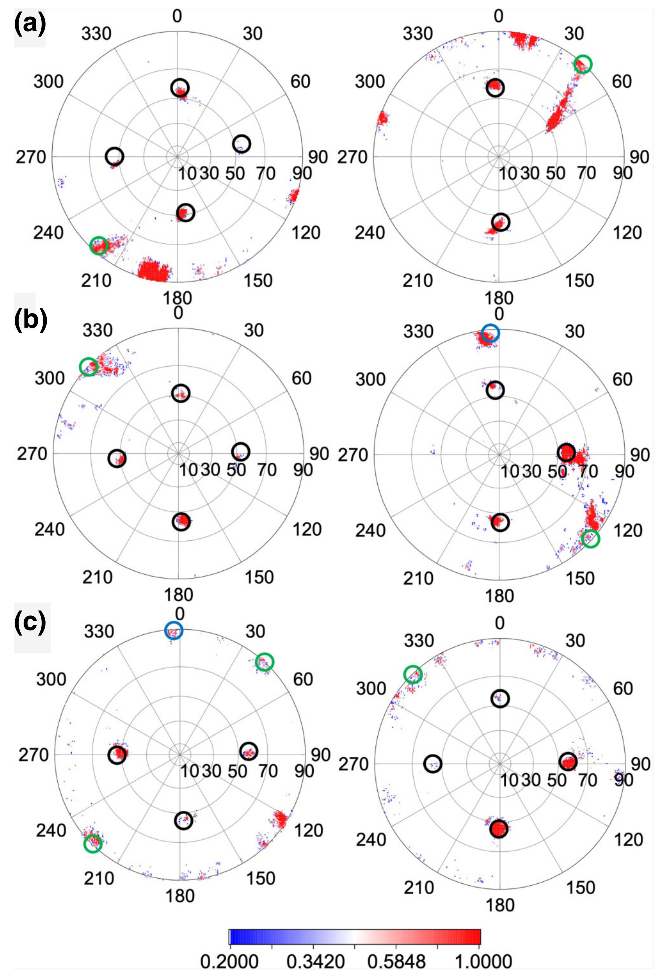

FIG. 4. South (left) and north (right) CXD pole figures extracted from diffraction patterns at $Q = 0.03$ Å^{-1} from the center of the Bragg peak from (a) NC 1 (b) NC 2, and (c) another crystal. The peaks corresponding to the {111}, {101}, and {100} facets are highlighted with black, blue, and green circles, respectively. All axes units are degrees.

usually occur in {111} crystallographic planes. SFs and twins may also contribute to the poles of the {111} type. Figure 4(c) shows pole figures from another nanocrystal on the sample. {101} streaks are observed. It is clear that the faceting is significantly different between each crystal, but the dominant facets are {111} as the size of the facet is also proportional to the intensity (see SEM images for more InP NCs in the Supplemental Material) [58].

IV. CONCLUSIONS

In conclusion, the NHE of InP on Si is shown to be a promising approach to grow high quality III-V nanomaterials for the monolithic integration of III-V-on-Si technology platform. GIXRD reveals the global properties of InP NCs while the characterization of a single InP NC using TEM is quite challenging due to the destructive lamella sample preparation. Combined with the nano-x-ray beam, the CXD measurements and analysis show detailed information on the crystal size, the facets, the single crystallinity, the location and directions of SFs (or μTW boundaries), and the size of μTWs of the single InP NC, which are in good agreement with the SEM, GIXRD, and TEM observations. Our approach paves a pathway to nondestructively and quantitatively explore the crystallographic properties and defects of semiconductor nanocrystals by offering a 3D structured imaging, which is of great significance to evaluate the quality of the active nanomaterials (even in an *operando* manner) of various fully processed, nano-electronic and nano-optoelectronic devices in the future.

ACKNOWLEDGMENTS

The authors acknowledge Jens Katzer and Hans-Micheal Krause for help on SEM measurements. We also gratefully acknowledge the assistance of Dr. Gilles Renaud and Dr. Maurizio De Santis at BM32 beamline of ESRF for the GIXRD measurements. The work is supported by the National Natural Science Foundation of China (Grant No. 51602247), the Deutsche Forschungsgemeinschaft (DFG) under “DACH” project (Grant No. SCHR 1123/10-1), the Natural Science Fundamental Research Project of Shaanxi Province of China (Grant No. 2017JQ6003), the Fundamental Research Funds for the Central Universities and the Natural Sciences and Engineering Research Council of Canada (NSERC DG Grant No. 203773).

[1] H. Attariani, K. Momeni, and K. Adkins, Defect engineering: a path toward exceeding perfection, ACS Omega **2**, 663 (2017).

[2] N. Shin, M. Chi, J. Y. Howe, and M. A. Filler, Rational defect introduction in silicon nanowires, Nano Lett. **13**, 1928 (2013).

[3] T. A. Taton and D. J. Norris, Defective promise in photonics, Nature **416**, 685 (2002).

[4] Q. Yan, L. Wang, and X. S. Zhao, Artificial defect engineering in three-dimensional colloidal photonic crystals, Adv. Funct. Mater. **17**, 3695 (2007).

[5] G. Niu, E. Hildebrandt, M. A. Schubert, F. Boscherini, M. H. Zoellner, L. Alff, D. Walczyk, P. Zaumseil, I. Costina, H. Wilkens, and T. Schroeder, Oxygen vacancy induced room temperature ferromagnetism in Pr-doped CeO_2 thin films on silicon, ACS Appl. Mater. Interfaces **6**, 17496 (2014).

[6] J. A. del Alamo, Nanometre-scale electronics with III-V compound semiconductors, Nature **479**, 317 (2011).

[7] E. P. A. M. Bakkers, J. A. van Dam, S. De Franceschi, L. P. Kouwenhoven, M. Kaiser, M. Verheijen, H. Wondergem, and P. van der Sluis, Epitaxial growth of InP nanowires on germanium, Nat. Mater. **3**, 769 (2004).

[8] A. J. Shields, Semiconductor quantum light sources, Nat. Photonics **1**, 215 (2007).

[9] T. Li, M. Mastro, and A. Dadgar, *III–V Compound Semiconductors: Integration with Silicon-Based Microelectronics* (Taylor & Francis, 2010).

[10] S. Mokkapati, C. Jagadish, and J. G. Webster, *Wiley Encyclopedia of Electrical and Electronics Engineering* (John Wiley & Sons, Inc., 1999).

[11] M. Sugo and M. Yamaguchi, Buffer layer effects on residual stress in InP on Si substrates, Appl. Phys. Lett. **54**, 1754 (1989).

[12] Z. Wang, B. Tian, M. Pantouvaki, W. Guo, P. Absil, J. Van Campenhout, C. Merckling, and D. Van Thourhout, Room-temperature InP distributed feedback laser array directly grown on silicon, Nat. Photonics **9**, 837 (2015).

[13] Y. T. Sun, G. Omanakuttan, and S. Lourdudoss, An InP/Si heterojunction photodiode fabricated by self-aligned corrugated epitaxial lateral overgrowth, Appl. Phys. Lett. **106**, 213504 (2015).

[14] M. Heurlin, P. Wickert, S. Fält, M. T. Borgström, K. Deppert, L. Samuelson, and M. H. Magnusson, Axial InP nanowire tandem junction grown on a silicon substrate, Nano Lett. **11**, 2028 (2011).

[15] P. D. Kanungo, H. Schmid, M. T. Björk, L. M. Gignac, C. Breslin, J. Bruley, C. D. Bessire, and H. Riel, Selective area growth of III–V nanowires and their heterostructures on silicon in a nanotube template: Towards monolithic integration of nano-devices, Nanotechnology **24**, 225304 (2013).

[16] D. Zubia and S. D. Hersee, Nanoheteroepitaxy: The application of nanostructuring and substrate compliance to the heteroepitaxy of mismatched semiconductor materials, J. Appl. Phys. **85**, 6492 (1999).

[17] G. Niu, G. Capellini, F. Hatami, A. Di Bartolomeo, T. Niermann, E. H. Hussein, M. A. Schubert, H.-M. Krause, P. Zaumseil, O. Skibitzki, G. Lupina, W. T. Masselink, M. Lehmann, Y.-H. Xie, and T. Schroeder, Selective epitaxy of InP on Si and rectification in graphene/InP/Si hybrid structure, ACS Appl. Mater. Interfaces **8**, 26948 (2016).

[18] O. Skibitzki, I. Prieto, R. Kozak, G. Capellini, P. Zaumseil, Y. A. R. Dasilva, M. D. Rossell, R. Erni, H. v. Känel, and T. Schroeder, Structural and optical characterization of GaAs nano-crystals selectively grown on Si nano-tips by MOVPE, Nanotechnology **28**, 135301 (2017).

[19] I. Prieto, R. Kozak, O. Skibitzki, M. D. Rossell, P. Zaumseil, G. Capellini, E. Gini, K. Kunze, Y. A. R. Dasilva, R. Erni, T. Schroeder, and H. v. Känel, Bi-modal nanoheteroepitaxy of GaAs on Si by metal organic vapor phase epitaxy, Nanotechnology **28**, 135701 (2017).

[20] H. Riel, L.-E. Wernersson, M. Hong, and J. A. d. Alamo, III-V compound semiconductor transistors-from planar to nanowire structures, MRS Bull. **39**, 668 (2014).

[21] I. Robinson and R. Harder, Coherent X-ray diffraction imaging of strain at the nanoscale, Nat. Mater. **8**, 291 (2009).

[22] K. M. Pavlov, V. I. Punegov, K. S. Morgan, G. Schmalz, and D. M. Paganin, Deterministic bragg coherent diffraction imaging, Sci. Rep. **7**, 1132 (2017).

[23] A. Yau, W. Cha, M. W. Kanan, G. B. Stephenson, and A. Ulvestad, Bragg coherent diffractive imaging of single-grain defect dynamics in polycrystalline films, Science **356**, 739 (2017).

[24] A. Ulvestad, M. J. Welland, W. Cha, Y. Liu, J. W. Kim, R. Harder, E. Maxey, J. N. Clark, M. J. Highland, H. You, P. Zapol, S. O. Hruszkewycz, and G. B. Stephenson, Three-dimensional imaging of dislocation dynamics during the hydriding phase transformation, Nat. Mater. **16**, 565 (2017).

[25] J. Miao, P. Charalambous, J. Kirz, and D. Sayre, Extending the methodology of X-ray crystallography to allow imaging of micrometre-sized non-crystalline specimens, Nature **400**, 342 (1999).

[26] M. A. Pfeifer, G. J. Williams, I. A. Vartanyants, R. Harder, and I. K. Robinson, Three-dimensional mapping of a deformation field inside a nanocrystal, Nature **442**, 63 (2006).

[27] M. C. Newton, S. J. Leake, R. Harder, and I. K. Robinson, Three-dimensional imaging of strain in a single ZnO nanorod, Nat. Mater. **9**, 120 (2009).

[28] W. Yang, X. Huang, R. Harder, J. N. Clark, I. K. Robinson, and H.-k. Mao, Coherent diffraction imaging of nanoscale strain evolution in a single crystal under high pressure, Nat. Comm. **4**, 1680 (2013).

[29] W. Cha, N. C. Jeong, S. Song, H.-j. Park, T. C. Thanh Pham, R. Harder, B. Lim, G. Xiong, D. Ahn, I. McNulty, J. Kim, K. B. Yoon, I. K. Robinson, and H. Kim, Core–shell strain structure of zeolite microcrystals, Nat. Mater. **12**, 729 (2013).

[30] V. Favre-Nicolin, F. Mastropietro, J. Eymery, D. Camacho, Y. M. Niquet, B. M. Borg, M. E. Messing, L. E. Wernersson, R. E. Algra, E. P. A. M. Bakkers, T. H. Metzger, R. Harder, and I. K. Robinson, Analysis of strain and stacking faults in single nanowires using bragg coherent diffraction imaging, New J. Phys. **12**, 035013 (2010).

[31] M. C. Newton, A. Parsons, U. Wagner, and C. Rau, Coherent X-ray diffraction imaging of photo-induced structural changes in $BiFeO_3$ nanocrystals, New J. Phys. **18**, 093003 (2016).

[32] M. Dupraz, G. Beutier, T. W. Cornelius, G. Parry, Z. Ren, S. Labat, M. I. Richard, G. A. Chahine, O. Kovalenko, M. De Boissieu, E. Rabkin, M. Verdier, and O. Thomas, 3D imaging of a dislocation loop at the onset of plasticity in an indented nanocrystal, Nano Lett. **17**, 6696 (2017).

[33] J. W. Kim, A. Ulvestad, S. Manna, R. Harder, E. E. Fullerton, and O. G. Shpyrko, 3D bragg coherent diffractive imaging of five-fold multiply twinned gold nanoparticle, Nanoscale **9**, 13153 (2017).

[34] V. L. R. Jacques, D. Carbone, R. Ghisleni, and L. Thilly, Counting Dislocations in Microcrystals by Coherent X-Ray Diffraction, Phys. Rev. Lett. **111**, 065503 (2013).

[35] M. J. Cherukara, K. Sasikumar, A. DiChiara, S. J. Leake, W. Cha, E. M. Dufresne, T. Peterka, I. McNulty, D. A. Walko, H. Wen, S. K. R. S. Sankaranarayanan, and R. J. Harder, Ultrafast three-dimensional integrated imaging of strain in core/shell semiconductor/metal nanostructures, Nano Lett. **17**, 7696 (2017).

[36] W. Mehr, A. Wolff, H. Frankenfeld, T. Skaloud, W. Höppner, E. Bugiel, J. Lärz, and B. Hunger, Ultra sharp crystalline silicon tip array used as field emitter, Microelectron. Eng. **30**, 395 (1996).

[37] G. Niu, G. Capellini, M. A. Schubert, T. Niermann, P. Zaumseil, J. Katzer, H.-M. Krause, O. Skibitzki, M. Lehmann, Y.-H. Xie, H. von Känel, and T. Schroeder, Dislocation-free Ge nano-crystals via pattern independent selective Ge heteroepitaxy on Si nano-tip wafers, Sci. Rep. **6**, 22709 (2016).

[38] G. A. Chahine, M.-I. Richard, R. A. Homs-Regojo, T. N. Tran-Caliste, D. Carbone, V. L. R. Jacques, R. Grifone, P. Boesecke, J. Katzer, I. Costina, H. Djazouli, T. Schroeder, and T. U. Schulli, Imaging of strain and lattice orientation by quick scanning X-ray microscopy combined with three-dimensional reciprocal space mapping, J. Appl. Cryst. **47**, 762 (2014).

[39] J. A. Venables, G. D. T. Spiller, and M. Hanbücken, Nucleation and growth of thin films, Rep. Prog. Phys. **47**, 399 (1984).

[40] S. Hertenberger, D. Rudolph, M. Bichler, J. J. Finley, G. Abstreiter, and G. Koblmüller, Growth kinetics in position-controlled and catalyst-free InAs nanowire arrays on Si(111) grown by selective area molecular beam epitaxy, J. Appl. Phys. **108**, 114316 (2010).

[41] S. Hara, T. Iida, Y. Nishino, A. Uchida, H. Horii, and H. I. Fujishiro, Selective growth of InSb on localized area of Si (100) by molecular beam epitaxy, J. Cryst. Growth **323**, 397 (2011).

[42] Q. K. K. Liu, N. Moll, M. Scheffler, and E. Pehlke, Equilibrium shapes and energies of coherent strained InP islands, Phys. Rev. B **60**, 17008 (1999).

[43] G. Niu, G. Capellini, G. Lupina, T. Niermann, M. Salvalaglio, A. Marzegalli, M. A. Schubert, P. Zaumseil, H.-M. Krause, O. Skibitzki, M. Lehmann, F. Montalenti, Y.-H. Xie, and T. Schroeder, Photodetection in hybrid single-layer graphene/fully coherent germanium island nanostructures selectively grown on silicon nanotip patterns, ACS Appl. Mater. Interfaces **8**, 2017 (2016).

[44] W. L. Winterbottom, Equilibrium shape of a small particle in contact with a foreign substrate, Acta Metall **15**, 303 (1967).

[45] Q. Li, B. Pattada, S. R. J. Brueck, S. Hersee, and S. M. Han, Morphological evolution and strain relaxation of Ge islands grown on chemically oxidized Si(100) by molecular-beam epitaxy, J. Appl. Phys. **98**, 073504 (2005).

[46] H. Gottschalk, G. Patzer, and H. Alexander, Stacking fault energy and ionicity of cubic III–V compounds, Phys. Status Solidi A **45**, 207 (1978).

[47] D. M. Hwang, S. A. Schwarz, T. S. Ravi, R. Bhat, and C. Y. Chen, Strained-layer Relaxation in Fcc Structures via the

Generation of Partial Dislocations, Phys. Rev. Lett. **66**, 739 (1991).

[48] R. Kozak, I. Prieto, Y. Arroyo Rojas Dasilva, R. Erni, O. Skibitzki, G. Capellini, T. Schroeder, H. von Känel, and M. D. Rossell, Strain relaxation in epitaxial GaAs/Si (001) nanostructures, Phil. Mag. **97**, 2845 (2017).

[49] M. Dupraz, G. Beutier, D. Rodney, D. Mordehai, and M. Verdier, Signature of dislocations and stacking faults of face-centred cubic nanocrystals in coherent X-ray diffraction patterns: A numerical study, J. Appl. Cryst. **48**, 621 (2015).

[50] O. Mandula, M. E. Aizarna, J. Eymery, M. Burghammer, and V. Favre-Nicolin, PyNX.Ptycho: A computing library for X-ray coherent diffraction imaging of nanostructures, J. Appl. Cryst. **49**, 1842 (2016).

[51] D. R. Luke, Relaxed averaged alternating reflections for diffraction imaging, Inverse Probl. **21**, 37 (2005).

[52] R. W. Gerchberg and W. O. Saxton, Phase retrieval by iterated projections, Optik **35**, 237 (1972).

[53] J. R. Fienup, Reconstruction of an object from the modulus of its fourier transform, Opt. Lett. **3**, 27 (1978).

[54] S. Marchesini, H. He, H. N. Chapman, S. P. Hau-Riege, A. Noy, M. R. Howells, U. Weierstall, and J. C. H. Spence, X-ray image reconstruction from a diffraction pattern alone, Phys. Rev. B **68**, 140101(R) (2003).

[55] J. N. Clark, X. Huang, R. Harder, and I. K. Robinson, High-resolution three-dimensional partially coherent diffraction imaging, Nat. Comm. **3**, 993 (2012).

[56] V. Favre-Nicolin, S. Leake, and Y. Chushkin, *Free Log-Likelihood As An Unbiased Metric for Coherent Diffraction Imaging*, arXiv:1904.07056 (2019).

[57] M.-I. Richard, S. Fernández, J. Eymery, J. P. Hofmann, L. Gao, J. Carnis, S. Labat, V. Favre-Nicolin, E. J. M. Hensen, O. Thomas, T. U. Schülli, and S. J. Leake, Crystallographic orientation of facets and planar defects in functional nanostructures elucidated by nano-focused coherent diffractive X-ray imaging, Nanoscale **10**, 4833 (2018).

[58] See Supplemental Material at http://link.aps.org/supplemental/10.1103/PhysRevApplied.11.064046 for (1) laboratory-based XRD results; (2) TEM sample fabrication challenges; (3) Si tips fabricaton process; (4) selective growth of InP NCs theory; (5) real space k-map; (6) more SEM images of InP NCs and (7) phase retrieval of one measured InP particle.

Correction: Email addresses for additional corresponding authors were inadvertently deleted during the production cycle and have now been inserted.